

Separating intrinsic and scattering attenuation in full waveform sonic logging with radiative transfer theory

Evert L. Durán,¹ Kasper van Wijk,² Ludmila Adam¹ and Irene C. Wallis¹

¹School of Environment, The University of Auckland, Auckland 1142, New Zealand. E-mail: edur409@aucklanduni.ac.nz

²Department of Physics, University of Auckland, Auckland 1142, New Zealand

Accepted 2018 January 16. Received 2017 November 14; in original form 2017 July 2

SUMMARY

Fitting the intensity of ensembles of sonic log waveforms with a radiative transfer model allows us to separate scattering from intrinsic attenuation in two wells of the Ngatamariki geothermal field, New Zealand. Independent estimates of scattering and intrinsic attenuation add to the geologic interpretation based on other well log data. Particularly, our estimates of the intrinsic attenuation confirm or refine inferences on fluid mobility in the subsurface. Zones of strong intrinsic attenuation in Well 1 correlate with identified feed zones in three of the six cases, and hint at permeability just above two of the other three zones. In Well 2, intrinsic attenuation estimates help identify all three identified permeable intervals, including a washout.

Key words: Fracture and flow; Hydrothermal systems; New Zealand; Downhole methods; Coda waves; Seismic attenuation.

1 INTRODUCTION

Seismic waves are sensitive to the physical properties of the subsurface. The physical parameters of interest to the geophysicist determine not only the phase of the seismic wave, but also its amplitude. With the improvements in the quality and quantity of seismic data, seismic amplitude analysis has developed into methods such as Amplitude Versus Offset (Rutherford & Williams 1989; Chapman *et al.* 2006), acoustic impedance inversion (e.g. Oldenburg *et al.* 1983; Riedel *et al.* 2009) and seismic wave attenuation analyses (e.g. Knopoff *et al.* 1964; Jackson & Anderson 1970; Rickett 2006, 2007; Jones 2013; Gamar-Sadat 2015, 2016).

Seismic wave attenuation has been a topic of geophysical research for several decades (e.g. Wyllie *et al.* 1962; Knopoff *et al.* 1964; O'Doherty & Anstey 1971; Spencer & Nur 1976; Johnston 1981; Dasios *et al.* 2001). In addition to geometric spreading, seismic waves attenuate due to two fundamentally different mechanisms. First, seismic energy can be converted to heat (commonly referred to as intrinsic attenuation, dissipation or absorption). A passing seismic wave distorts the pore pressure by changing the state of stress. This local change of stress produces pressure gradients that trigger the mobility of fluids and hence absorption (dissipation) of the wavefield energy (Pride *et al.* 2004; Adam *et al.* 2009; Müller *et al.* 2010; Vinci *et al.* 2014). Several theories deal with the mechanisms that explain the mobility of fluids in the pore space, such as global fluid flow and squirt flow mechanisms (Biot 1956; Toksöz *et al.* 1979; Mavko & Jizba 1991; Dvorkin *et al.* 1995). Internal friction between grain contacts and cracks has also been reported as an attenuation mechanism in the literature (Attewell & Ramana 1966; Walsh 1966; Johnston *et al.* 1979; Winkler *et al.* 1979). For this mechanism, however, attenuation increases with increasing strain

magnitude, but is commonly ignored for small strains ($<10^{-6}$). Such strains are of the magnitude exerted by propagating elastic waves.

Second, seismic waves attenuate as they scatter out of the direction of propagation upon encountering impedance contrasts, either as Rayleigh scattering when the scatterers are smaller than the wavelength or Mie scattering when they are of similar size to the wavelength. In solids these contrasts are provided by common geological features such as lamination, layering, fractures and clasts.

This combination of attenuation mechanisms of seismic waves is typically quantified by the quality factor Q . It is related to the attenuation coefficient α as: $Q = \alpha v / \pi f$ (Knopoff 1964), with v being group velocity and f the frequency of the wave. The factor α controls the exponential decay of a plane wave with distance. The most common method to estimate attenuation from seismic data is by computing spectral ratios of the first arrivals (Toksöz *et al.* 1979). However, Toksöz *et al.* (1979) and Parra *et al.* (2007) point out that wave reflections and scattering can introduce oscillations in the amplitude spectra of the waveform, complicating the estimation of attenuation from spectral ratios. In addition, Gurevich & Pevzner (2015) show that since attenuation is frequency dependent as a power law, spectral ratio estimates become biased (i.e. when $Q^{-1} \propto \omega^n$, then Q is systematically underestimated by a factor of $n + 1$). However, even when the utmost care is taken to estimate attenuation from spectral ratios, this methodology is not able to separate intrinsic from scattering attenuation. Losses due to the latter have been modelled with elastic wave propagation through a multiple scattering medium composed of thin layers (O'Doherty & Anstey 1971; Shapiro *et al.* 1994; Van Der Baan 2001). Recent applications of this approach coupled with the modified centroid frequency shift method can be found in Pevzner (2016).

Scattering attenuation has been analysed through the use of coda waves or the late superposition of arrivals (backscattering) in the seismic record (Aki & Chouet 1975). Herraiz & Espinosa (1987) offer a review of the first attempts to understand seismic scattering from the late part of seismological records. Margerin (2005) covers the use of Radiative Transfer theory to model the regime of multiple scattering responsible for the coda. This theory has been applied to model scattering and intrinsic attenuation at the scale of lithospheric (Fehler *et al.* 1992; Sato & Fukushima 2013; Mayor *et al.* 2014; Sato & Hayakawa 2014) to mantle heterogeneities (Sato & Nishino 2002; Margerin & Nolet 2003). Our aim is to separate the contribution from intrinsic and scattering attenuation of waves at a smaller scale, namely in sonic Stoneley waves in boreholes of a geothermal field in New Zealand. Stoneley waves are generated in the interface between two solid elastic media (Stoneley 1924) and decay exponentially in amplitude away from the fluid-solid boundary of the borehole (Cheng *et al.* 1982). These waves can reflect from large open fractures, and this reflectivity can be related to their aperture (Hornby 1989). In the borehole logging community Stoneley waves are commonly referred to as tube waves or guided waves.

Ultimately, for the production of geothermal (and hydrocarbon) reservoirs, we are particularly interested in characterizing the mobility of fluids (permeability) (Klimentos & McCann 1990; Pride *et al.* 2003). Stoneley waves are highly attenuated in fractured areas and their transmission and reflection coefficients are sensitive to fluid transport (Tang & Cheng 1989; Hornby *et al.* 1989). Nevertheless, Stoneley waves are affected by a combination of permeability changes, rock alteration, and scattering from lithological discontinuities. The challenge is to separate these effects (Hardin *et al.* 1987). Stoneley waves have been used in acoustic borehole logging to study their relation to rock permeability (Cheng *et al.* 1982; Winkler *et al.* 1989; Kostek *et al.* 1998a,b; Tang & Cheng 2004). A common approach is to forward model the propagation of Stoneley waves in the presence of layering and fractures (Cheng & Toksöz 1981; Hornby *et al.* 1989; Frehner & Schmalholz 2010; Karpfinger *et al.* 2010; Bakku *et al.* 2013; Sinev & Podbereznyy 2013). Hornby *et al.* (1989) and Kostek *et al.* (1998a,b) show that open fractures can be detected using full waveform sonic logs by studying the coherent Stoneley wave arrival. However, when the geology is composed of cross-cutting fractures in the presence of strong layering, or laminations, and veins, this approach is not easy to implement. This is because the Stoneley wave reflectivity will be affected by interference from all these features, masking the correlation of amplitudes to simple fracture models. What we propose is to fit the intensity of the full waveform sonic logs (FWSL) as a function of space and time with a 1-D radiative transfer model. This way, we can separate scattering from intrinsic attenuation to help identify permeable regions in the subsurface. We first introduce the radiative transfer theory, then estimate scattering and intrinsic attenuation as a function of depth in two injection wells of Ngatamariki geothermal field in New Zealand (Fig. 1), present their geological interpretation and discuss the results.

2 METHOD

Radiative transfer theory (RT) describes the evolution of the intensity of a wavefield, which has its origins in the kinetic theory of gases (Schuster 1905; Chandrasekhar 1960, 2013). RT allows us to separate scattering and absorptive properties of the medium within a region where the properties of the medium are stationary. The

group of wavefields recorded in such region forms an *ensemble*. The coherent intensity decays with distance travelled due to scattering and absorption. Scattering, however, results in an incoherent intensity, often described as ‘coda’ in seismology. If heterogeneity is strong, multiple scattering can act as a gain term for the coda (Wu 1993). One strategy to separate scattering from intrinsic losses is to perform full-waveform inversion, but particularly in the case of strong scattering, this would be a formidable challenge. Instead, we will take the approach to find the scattering and absorption losses in the ensemble that describe the total intensity of the wavefield. The derivation of the analytic solution to 1-D RT equations can be found in Paasschens (1997) and Haney *et al.* (2005). Therefore, we will only state the results here.

The square of the average wavefield impulse response $G(x, t)$ is known as the coherent intensity, CI (e.g. Ishimaru 2013), and in 1-D is

$$CI(x, t) = \langle G(x, t) \rangle^2 = \exp(-vt(R/l_s + 1/l_a))\delta(x - vt), \quad (1)$$

where x and t are the source-receiver offset and time respectively, v is the velocity of the coherent intensity (group velocity) and the two parameters that describe the losses of intensity are the mean-free path for absorption l_a and the mean-free path for scattering l_s . These lengths represent the average distance required for the intensity to decay to a value of $1/e$. The scattering mean free path l_s is coupled with a dimensionless parameter R describing the proportion of energy backscattered from impedance contrasts (Haney *et al.* 2005). Eq. (1) allows the estimation of the decay of the intensity from the cumulative effect of absorption l_a and scattering R/l_s . For a causal source wavelet $s(t)$, Appendix A shows that the coherent intensity is

$$CI(x, t) * s(t) = \exp(-x\alpha)s(t - x/v). \quad \alpha = R/l_s + 1/l_a. \quad (2)$$

The total intensity TI is the average of the square of the wavefield (Haney *et al.* 2005):

$$TI(x, t) = \langle G^2(x, t) \rangle = \exp(-vt(R/l_s + 1/l_a)) \times \left[\delta(x - vt) + \frac{R}{2l_s} \left(I_0(\eta) + \sqrt{\frac{vt+x}{vt-x}} I_1(\eta) \right) \right], \quad (3)$$

where the argument $\eta = \frac{R}{l_s} \sqrt{(vt)^2 - x^2}$ of the Modified Bessel functions of the first kind (I_0 and I_1) only depends on scattering, and not absorption. That is why the Modified Bessel functions of the first kind describe a gain term in the total intensity; waves originally scattered out of the coherent intensity are scattered back into the incoherent intensity (van Wijk 2003; Haney *et al.* 2005). The incoherent intensity, II, of the field is the difference between the total and coherent intensities:

$$II(x, t) = TI - CI = \exp(-vt(R/l_s + 1/l_a)) \times \left[\frac{R}{2l_s} \left(I_0(\eta) + \sqrt{\frac{vt+x}{vt-x}} I_1(\eta) \right) \right]. \quad (4)$$

Our strategy is to fit the observed intensities of full-waveform sonic logging data in order to obtain individual estimates of the scattering and absorption mean free path. In seismology, however, attenuation is more commonly described through the quality factor Q , a dimensionless parameter describing wave amplitude loss per cycle (Futterman 1962; Knopoff 1964; O’Connell & Budiansky 1978; Pride *et al.* 2004; Toverud & Ursin 2005). The quality factors relate to the mean free paths after Haney *et al.* (2005) as

$$Q_a = \frac{2\pi f l_a}{v}, \quad Q_s = \frac{2\pi f l_s}{v}, \quad (5)$$

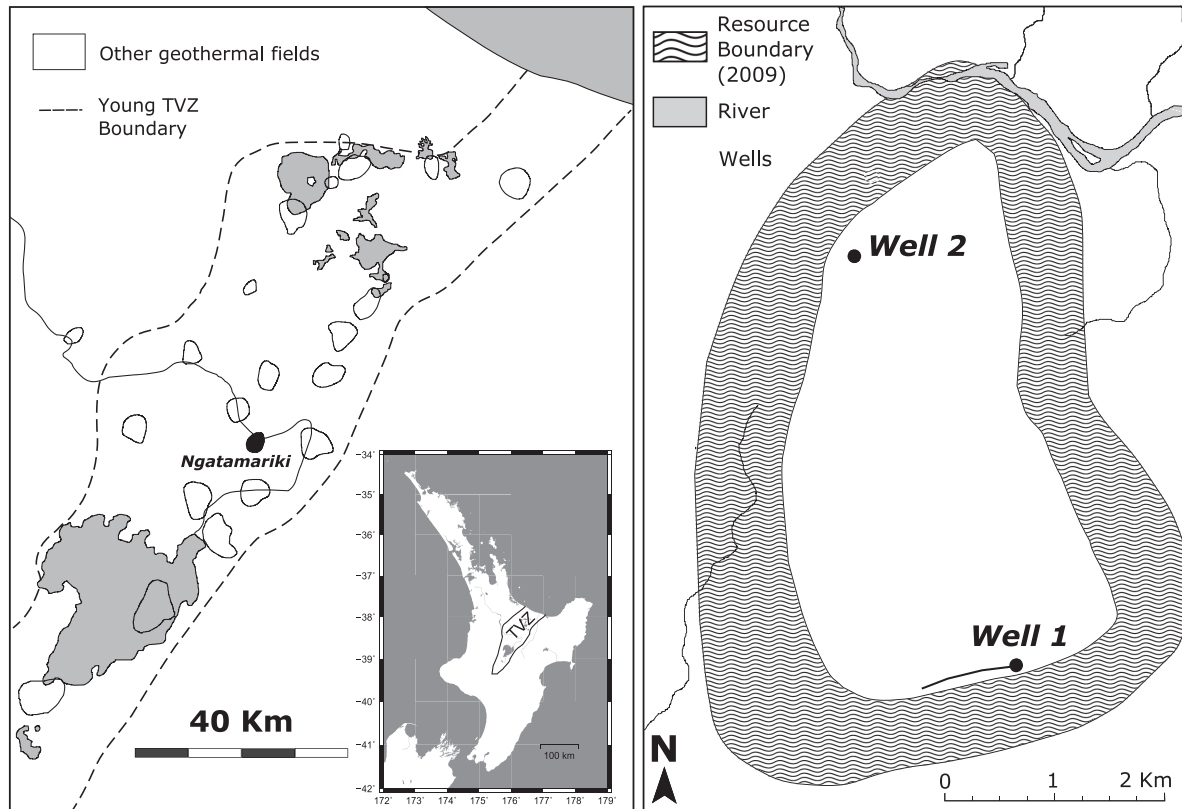


Figure 1. Left: location of Ngatamariki in the North Island of New Zealand (shown in black). The field is in the Taupo Volcanic Zone (TVZ). The Young TVZ boundary is after Wilson *et al.* (1995). Right: position of the wells in the field. Field boundaries are as determined by Mercury NZ Ltd in 2009.

where f is the dominant wave frequency and v is the group velocity of the energy propagating in the medium.

The work flow to estimate Q_a and Q_s as a function of depth is as follows:

- (i) Group waveforms in ensembles that represent stationary geological intervals.
- (ii) Compute the coherent, total and incoherent intensities for each ensemble, according to eqs (1), (3) and (4), respectively.
- (iii) Estimate the group velocity v from the coherent intensity.
- (iv) Estimate the mean free paths l_s and l_a from a least-squares fit to the observed coherent and incoherent intensities.
- (v) Estimate the quality factors Q_a and Q_s from eq. (5).

All our results and interpretations are done in the framework of a 1-D RT analysis, based on the assumption that wave propagation is dominated by up- and downgoing Stoneley waves; the strongest wave in the record. Some of this Stoneley wave energy is scattered to body waves, not included in our current analysis. Body wave energy not returning to the receiver adds to the loss term, captured by intrinsic absorption. Future work will include expansion to a higher-dimensional RT analysis to account for body-wave scattering in other directions than the vertical.

2.1 Example

Fig. 2 presents an example ensemble of 16 sonic waveforms at fixed source–receiver distance recorded over a 2.4 m interval. Each waveform is $u(x, t) = s(t) * G(x, t)$, where x is the vertical distance between source and receiver, and the $*$ symbol represents the convolution of the source wavelet $s(t)$ with the impulse response

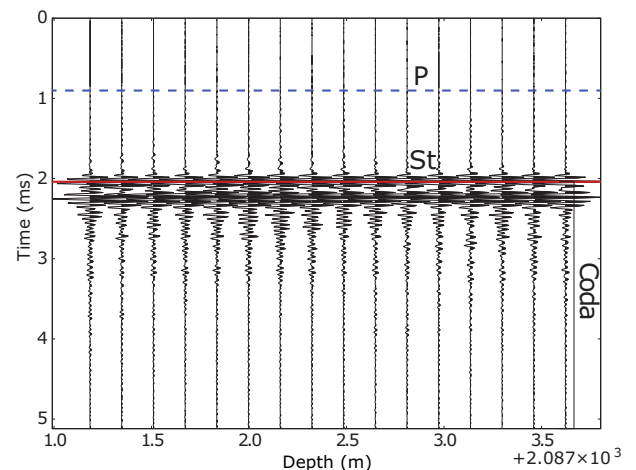


Figure 2. The ensemble of traces for the first receiver for the depth interval between 2088.2 and 2090.6 m in Well 1, where the direct primary wave (P) and Stoneley wave (St) arrivals are followed by scattered waves in the coda.

$G(x, t)$. A weak direct P -wave arrives at $t = 1$ ms, followed by a much stronger Stoneley wave around $t = 2$ ms. The arrivals after the Stoneley wave form the coda; a superposition of waves scattered by interactions with the medium heterogeneities.

The coherent intensity for this ensemble is obtained by taking the average ('stack') of the wavefields in the ensemble, and squaring the result: $\langle u(x, t) \rangle^2$. The coherent intensity is dominated by constructively interfering direct waves for each realization in the ensemble. We compute this intensity for all eight receivers (Fig. 3). The maximum of the natural logarithm of the coherent intensity for

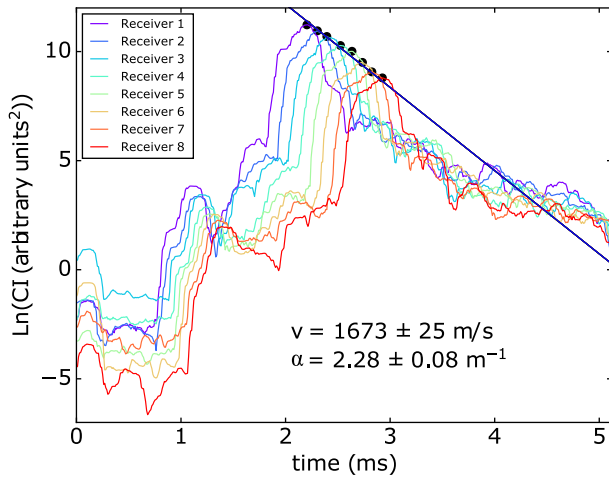


Figure 3. Coherent intensity decay for receivers in an ensemble. The model fits the exponential decay of the coherent intensity. The ensemble group velocity is also estimated from the arrival times of coherent intensity for the eight receivers.

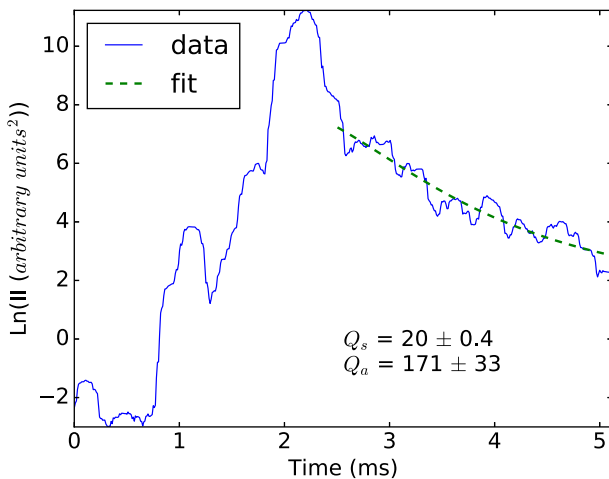


Figure 4. Incoherent intensity and best-fitting model, described by eq. (4).

each receiver position is represented by the dots in Fig. 3. These maxima provide an estimate of the exponential decay in eq. (1), and the Stoneley wave group velocity v follows from the arrival time of the maximum as a function of distance. For this ensemble, $v = 1673 \pm 25 \text{ m s}^{-1}$, and $1/l_a + R/l_s = \alpha = 2.28 \pm 0.08 \text{ m}^{-1}$.

The incoherent intensity decays less than exponential due to gain from multiply scattered seismic waves (Fig. 4). The least-squares fit (thick dashed line) to the equation for the incoherent intensity (eq. 4) results in an estimate of $l_s = 0.27 \pm 0.01 \text{ m}$. This estimate was obtained assuming isotropic scattering ($R = 0.5$) (Haney *et al.* 2005). With eq. (5) and a dominant sonic log frequency of 20 kHz, we estimate $Q_s = 20 \pm 0.4$ for this ensemble. By combining the $1/l_a + R/l_s$ information from the coherent energy, we estimate $l_a = 2.28 \pm 0.08 \text{ m}$ and eq. (5) leads to an estimate of $Q_a = 171 \pm 33$. We refer the reader to Appendix B for details on error estimation and propagation. These estimates imply that attenuation is dominated by scattering. We will see that this is common in the well logs in this study. Therefore, it is clear that to reveal fluid processes in the subsurface we need independent estimates of scattering and intrinsic attenuation.

3 RESULTS

The Ngatamariki field is located in the Taupo Volcanic Zone (TVZ), New Zealand (Fig. 1). The TVZ is of interest to the geothermal industry and to geologists in general due to its high heat flow and the large volume of volcanic deposits accumulated during a relatively short period of time (Wilson *et al.* 2009). The field has an installed geothermal power capacity of 82 MW and the success of the fluid production and reinjection in the field depends on permeable intervals in the volcanic sequence. The Tahorakuri Formation is the main reservoir hosting unit of the Ngatamariki geothermal field (Wallis *et al.* 2009; Boseley *et al.* 2012), composed of a thick (0.8–1.7 km) section of silicic primary volcanic and secondary volcanoclastic rocks (Chambefort *et al.* 2014). The permeability of Tahorakuri samples range from 9.8×10^{-21} to $2.4 \times 10^{-16} \text{ m}^2$, and the matrix permeability is attributed to rock microfractures and connected pore throats (Cant 2015). Fractures, however, also play a role in the fluid flow in the Tahorakuri Formation. Underlying the Tahorakuri Formation, the Ngatamariki Andesite is a sequence of andesitic lava flows with a high density of fractures. Fig. 1 shows the field location and current wells. The two wells used in this study are Well 1 in the southern part of the field, and Well 2 to the North.

3.1 Well 1

Following the RT methodology described, we estimate attenuation parameters as a function of depth. Figs 5 and 6 present estimates of the group velocity v , and attenuation (Q_s , Q_a and Q_t) for Wells 1 and 2, respectively. The uncertainties are discussed in Appendix B, where we point that longer recording times may reduce uncertainties in future studies of this kind.

In Well 1, Q_s oscillates between 11 ± 2 and 164 ± 120 with a median value of 21. Larger variability is observed in Q_a with a median value of 191. The total quality factor is dominated by scattering, as can be seen that Q_t and Q_s generally correlate with depth.

On the larger scale, the RT analysis reveals a break in characteristics at 2500 m. This depth represents the contact between the Tahorakuri Formation (above) and the Ngatamariki Andesite (below). In the Tahorakuri Formation, group velocity is fairly constant, while Q_t and Q_s decrease slowly. In the underlying Ngatamariki Andesite, these three parameters become more variable, but appear to increase overall. Intrinsic attenuation estimates have larger uncertainties, but local fluid mobility information is hidden in a distinct Q_a behaviour, discussed in the next section.

3.2 Well 2

The data from Well 2 in Fig. 6 are restricted to the Tahorakuri Formation, with RT parameters that generally match the attenuation estimates in the same Tahorakuri Formation in Well 1. Q_s goes from a minimum of 10 ± 1 to a few values above 3000 with a median of 22. On the other hand, Q_a oscillates between 16 ± 1 and a high value of 800 with considerable error bars. The median Q_a is 179.5. We next discuss our estimates of attenuation in the context of other available data sets such as geophysical well logs and spinner tool.

4 DISCUSSION

Sonic and electrical logs allow for the correlation of geological contacts, identification of secondary mineralization, and estimation

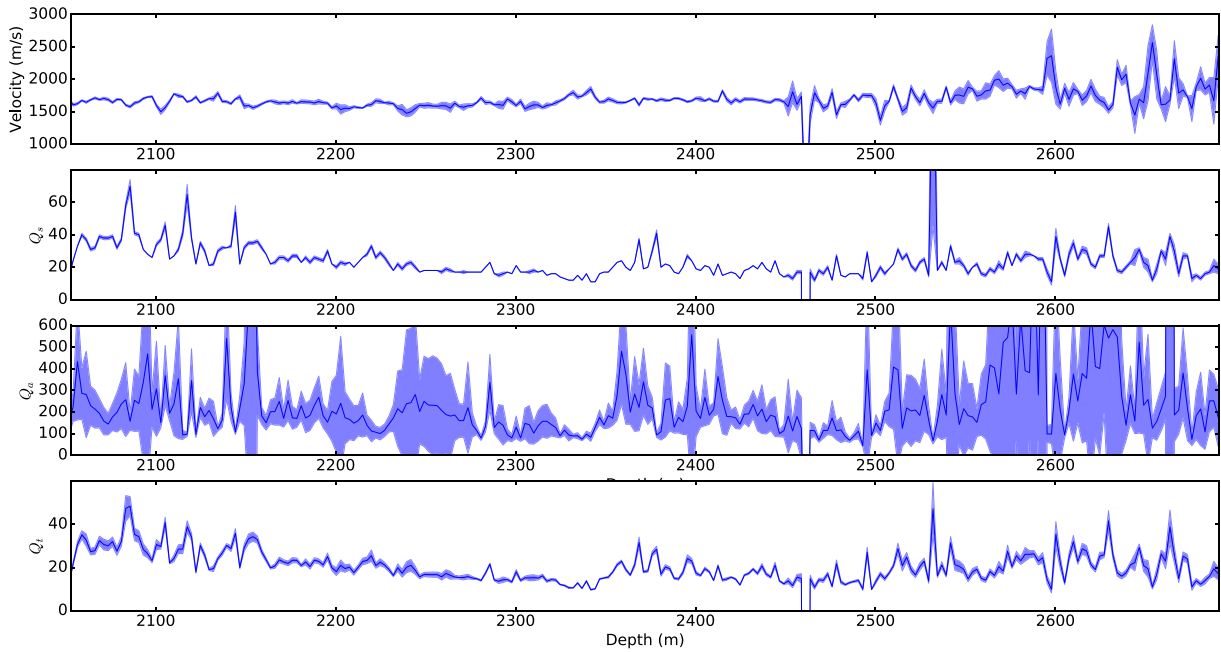


Figure 5. Mean (line) and standard deviation (shading) of group velocity v , scattering attenuation Q_s , intrinsic attenuation Q_a and total attenuation Q_t estimates in Well 1.

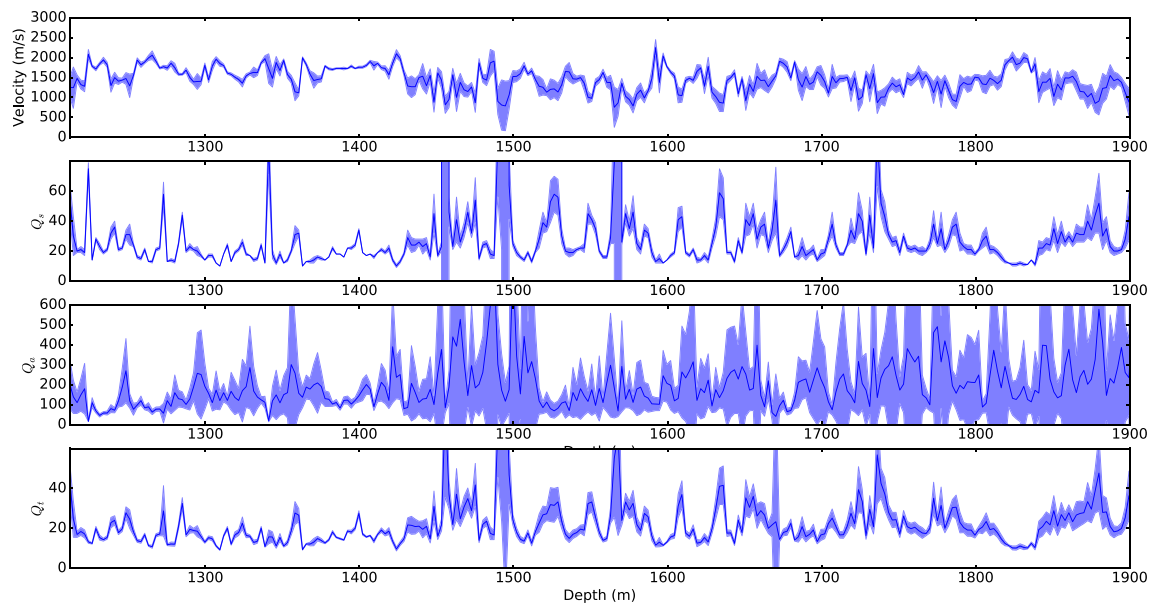


Figure 6. Mean (line) and standard deviation (shading) of group velocity v , scattering attenuation Q_s , intrinsic attenuation Q_a and total attenuation Q_t estimates in Well 2.

of rock physical properties for geomechanical modelling (Wallis *et al.* 2009). Here, we explore the (hydro)geologic implications of the attenuation estimates in Wells 1 and 2, within the context of complementary (well log) data. Particularly, we focus on the value of individual estimates of intrinsic and scattering attenuation.

4.1 Well 1

Formation Micro Imager (FMI) logs discussed in Appendix C1 were used to estimate density and aperture of fractures, as well as the facies and textures in Well 1. Panel (a) in Fig. 7 depicts the textures interpreted from FMI (Halwa *et al.* 2013; Halwa 2012).

Red indicates fractured, green is banded, and blue represents clastic. Electric resistivity logs are shown in panel (b). Shallow and deep resistivity logs follow similar trends in the Tahorakuri Formation, but the tool that senses deeper reads lower resistivity values. In the Ngatamariki Andesite, deep and shallow resistivity logs show similar values, which implies the continuity of the electrical response past the borehole wall. P - and S -wave sonic slowness are shown in panel (c). Overall, the S -wave sonic log presents greater variability with depth than the P -wave slowness. Fracture density interpreted from the FMI log is shown in panel (d). The Tahorakuri Formation is dominated by a lower density of fractures of small to large aperture, while the Ngatamariki Andesite has a higher count of fractures of small aperture. The lower part of the Ngatamariki Andesite hosts

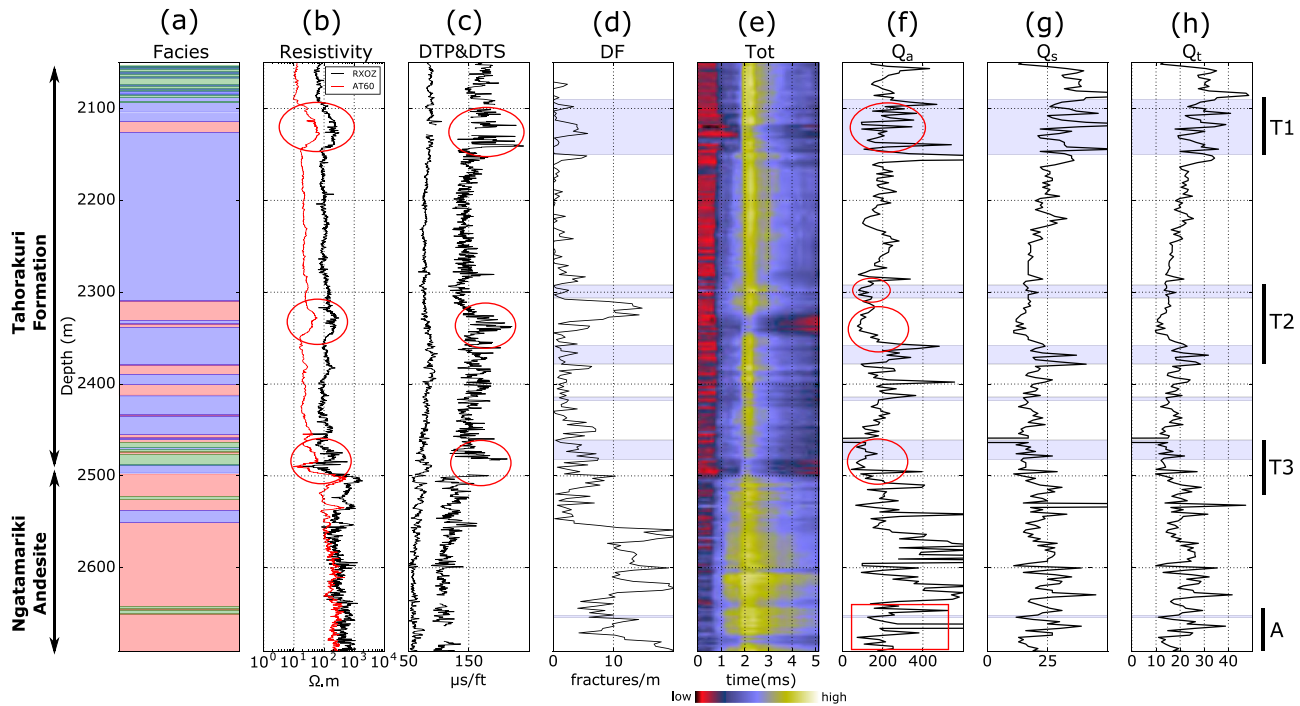


Figure 7. Well log data for Well 1. The colours in panel (a) represent the textures interpreted from FMI images (Halwa 2012). Red: fractured. Green: banded. Blue: clastic. (b) Shallow resistivity (RXOZ) and deep induction resistivity (AT60). (c) Sonic slownesses for P and S -wave arrivals (DTP & DTS). Density of fractures (d), total intensity of ensemble (e) and Q_a (f), Q_s (g) and Q_t (h). Previously interpreted feed zones are indicated by blue transparent bands in the attenuation panels.

intervals of significant circulation losses, with no cutting returns. The total intensity of the FWSL is depicted in panel (e). The background noise level in the total intensity panel is the red colour, before the P -wave arrival at approximately 0.8 ms. The intensities associated with the dominant Stoneley waves start at ~ 2 ms in yellow. The TI decays after the arrival of the Stoneley wave, but this intensity decay is variable with depth, and forms the source of group velocity and attenuation estimates. The mean values of the attenuation estimates of Fig. 5 are repeated in Figs 7(f)–(h). Feed zones are marked as blue transparent bands in the quality factor panels. These zones are based on fluid velocities calculated from a Pressure Temperature Spinner (PTS) tool, using three different pressure rates and taking into account fluid viscosity and borehole irregularities. However, the cut-off details on flow are unavailable.

Generally, the dominant attenuation mechanism in Well 1 is scattering due to heterogeneity identified in the FMI from the clasts, veins, layering and fractures. These features introduce significant impedance contrasts that scatter sonic waves. There is a distinct change in the TI pattern at 2500 m (Fig. 7e), resulting from the sharp lithological change between the Tahorakuri Formation and the Ngatamariki Andesite. The andesite is regarded as an injection interval due to its alternating fracture characteristics and long intervals of total circulation losses. On average, the andesite shows high values of Q_a (low absorption), while the pyroclastic Tahorakuri Formation—intrinsically porous and permeable—shows low average Q_a estimates. Within the Tahorakuri Formation, we observe positive correlations between the feed zones, and zones of low values of Q_a . These areas occur in intervals interpreted from the FMI images as fractured predominantly, and banded secondly. Three intervals within the Tahorakuri Formation, 2090–2150 m (T1), 2310–2390 m (T2) and 2470–2510 m (T3) are discussed next to explore the interpretations from the RT results in greater detail.

4.1.1 Tahorakuri Formation

T1, T2 and T3 in Fig. 7 are identified as high fluid flow areas within the Tahorakuri Formation by the PTS tool. In addition, T1 and T2 show a decrease in shear wave velocity, strong absorption (low Q_a), and an increase in resistivity. The decrease in wave speed (high slowness log value) and high absorption point at an increase in fractures in the T1 and T2 intervals. The presence of fractures results on a more compliant rock, reducing wave speeds. We highlight these low speed intervals and their correlation to low Q_a with red ellipses in panels (c) and (f) in Fig. 7. These intervals also qualitatively correlate with the high fracture count intervals interpreted from the FMI log (Fig. 7d).

If open fractures are saturated with a conductive fluid, electrical resistivity is expected to be low. Resistivity however, is high in T1 and T2 intervals (Fig. 7b). In interval T3 the resistivity decreases, fracture count increases, and fluid losses were reported while drilling. At the base of this interval is the transition from Tahorakuri to the Ngatamariki Andesite. Resistivity logs are challenging to interpret in geothermal environments. The drilling fluid is fresh water, but *in situ* fluids charged with a variety of ions complicate the interpretation of the resistivity of the fluid. In addition, mineral alteration can significantly affect the interpretation of resistivity logs. Alteration to quartz in veins in the Tahorakuri formation in Well 1 has been reported, while Well 2 has clay, pyrite and quartz alteration, all of which affect the interpretation of electrical resistivity in the rock matrix.

Interval T1 displays the highest values of Q_s within the Tahorakuri Formation, and high intrinsic attenuation correlates with a high density of fractures. At T2 there is a match between the densely fractured region identified on FMI images and the highest absorption attenuation intervals. We argue that some of the

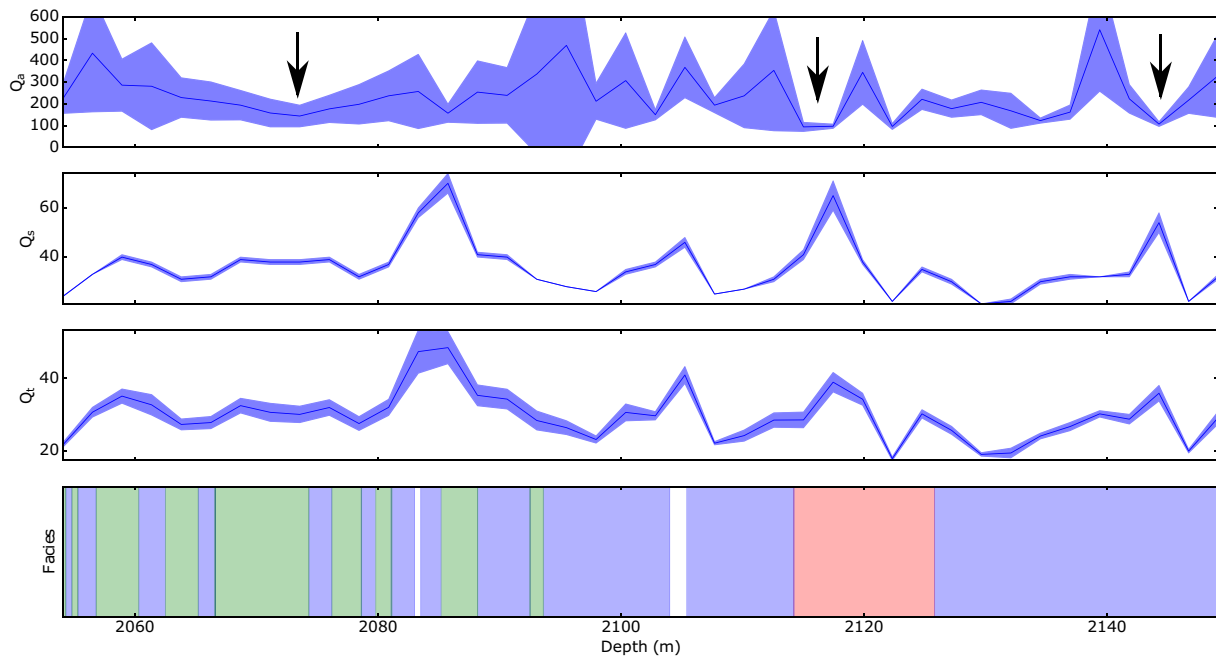


Figure 8. Attenuation estimates for Well 1 above and over the permeable interval T1. The intervals considered high in intrinsic attenuation are shown by the arrows.

fractures estimated by the FMI logs might be filled with conductive minerals, reducing or stopping fluid flow. The fracture count does not necessarily correlate with the highest absorption, which makes the Q_a log an independent tool of fluid flow interpretation.

All three feed zones contain ensembles with strong intrinsic attenuation, and it may be that the RT analysis helps constrain the actual depth of the source of fluid flow within a PTS-defined feed zone. To highlight the potential of RT attenuation estimates, Fig. 8 displays attenuation estimates for the permeable T1 interval shown in Fig. 7. Here too, the total attenuation is dominated by scattering, which correlates well with transitions in facies, leading to impedance contrasts necessary for the scattering of elastic waves. Black arrows around 2118 and 2142 m point to regions where scattering is *relatively* weak, but intrinsic attenuation relatively strong; these are possibly the actual source points of the T1 feed zone. The third option for a source of fluids is a region of relatively low values of Q_a just above the defined T1 feed zone (2070 m).

4.1.2 Ngatamariki Andesite

We interpret the highest values of Q_a as sections of competent andesite. Strong variability in attenuation confirms the variability in the fractured sections. The Andesite has one identified feed zone within the region annotated with an ‘A’ in Fig. 7. This thin zone agrees with an ensemble with low quality factors indicating scattering and intrinsic losses.

4.2 Well 2

Fig. 9 summarizes the well log information in Well 2. The data only sample the Tahorakuri Formation in a non-producing interval, where alteration increases with depth due to an intrusion below. Panel (a) depicts the lithological boundaries taken from geological reports, based on drill cuttings, cores, thin sections, and the response of the well logs. Panel (b) is the caliper log, showing a significant

washout section at ~ 1400 m. The shallow and deep resistivity logs in panel (c) show similar trends, with a slight separation towards the deeper and more altered Tahorakuri section. Panel (d) contains the P - and S -wave slowness sonic logs, with similar responses with depth. Panels (e) to (h) show the total intensities for the FWSL and the quality factors. From 1208 to 1425 m, the total intensity decays relatively fast with time. Below 1425 m the total intensity decays more slowly, indicated by the high intensity (yellow colour) persisting at late times. As for Well 1, the scattering component generally dominates the total quality factor.

The main geological factors contributing to the variability of the logs in this well are the different welding levels of the pyroclastic materials and the geothermal mineral alteration. In the presence of conductive minerals (e.g. clays, pyrite or iron oxides) special care must be taken when interpreting the electrical logs and their relation to fluid content. Therefore we interpret the combined effects of electrical and acoustic/elastic logs. Next, we discuss three regions of interest in Fig. 9: a washout area (W), a fractured welded ignimbrite (WI) and a feed zone (F) corresponding to the lowest values of Q_a in the well.

4.2.1 Washout

From 1380 to 1425 m—annotated with a ‘W’—we observe consistently low values in Q_a . At this geological interval there has been significant water loss while drilling (Wallis *et al.* 2009). This section is not defined as a feed zone, but clearly one affected by fluid flow; the caliper log indicates the presence of a washout, further corroborated by a decrease in compensated sonic logs. The resistivity logs show a decrease in resistivity, but these measurements could be affected by the borehole diameter. This interval also has the highest pyritic alteration of the whole log. Pyrite alteration decreases with depth, replaced by an increase in quartz alteration, each potential reasons for the variations in resistivity besides fluid content.

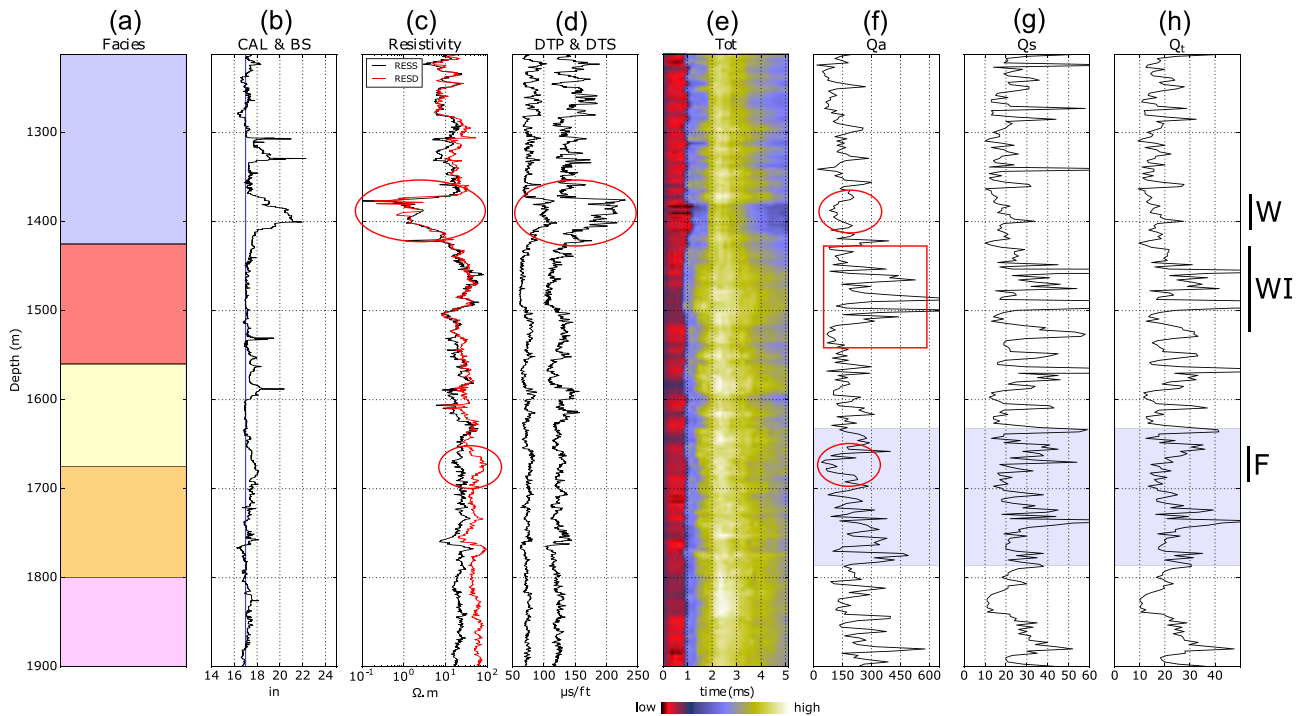


Figure 9. A compilation of well logging data in Well 2. The background colours in panel (a) represent the geological intervals encountered: breccia tuff (blue), welded ignimbrite (red), tuff and polymictic volcanoclastic breccia (yellow), veined tuff breccia (orange) and partially welded crystal-poor tuff (purple). (b) Caliper and bit size (CAL & BS). (c) Shallow and deep resistivity (RESS, RESD). (d) Sonic P - and S -wave slowness (DTP & DTS). (e) Total sonic log intensity (TI), and Q factors: (f) Q_a , (g) Q_s and (h) Q_t . Feed zone intervals are indicated by blue transparent bands in the panels with Q factors.

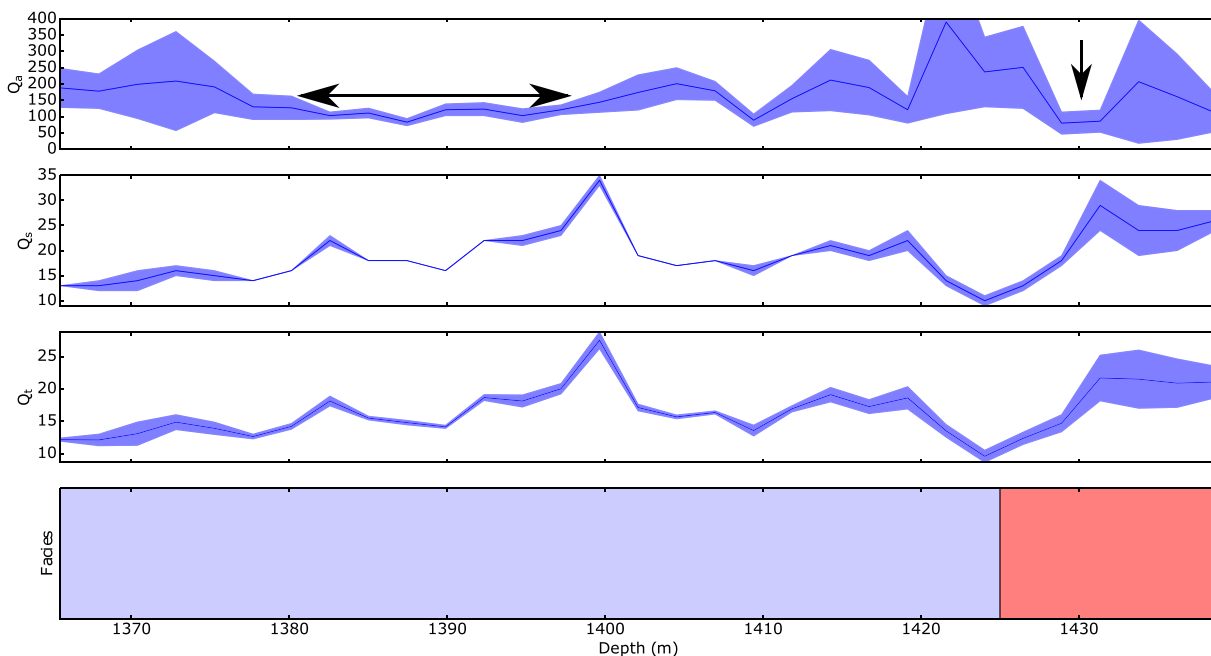


Figure 10. Attenuation estimates for the washout zone in Well 2. The intervals considered high in intrinsic attenuation are shown by the arrows.

4.2.2 Welded Ignimbrite

At 1425 m depth, a hard, crystal- and shard-rich welded and fractured ignimbrite is encountered (red box in Fig. 9 f annotated with a ‘WI’). Scattering of the FWSL in this region is attributed to veining, welding, fracture and alteration in this part of the Tahorakuri Formation. High drilling fluid losses are reported for the upper part of

the welded ignimbrite (Wallis *et al.* 2009). These losses comprise the interval between 1400 m and 1500 m depth. Low Q_a values correlate to this area of high fluid loss. However, the resistivity and sonic logs show insignificant changes in this zone.

Fig. 10 covers attenuation estimates from ‘W’ to ‘WI’. Strong intrinsic attenuation is indicated by the double arrow between 1380 m

and 1400 m. Total Q is dominated by scattering, and does not identify the washout. The next relevant interval with high absorption is at the top of the welded ignimbrite (1430 m), seen as a local minimum in the Q_a log. Scattering attenuation in this section actually decreases, as we transition from tuff to welded ignimbrite.

4.2.3 Feed zone

Below the welded ignimbrite, quartz alteration and intermittent welding dominate. At 1632 m the top of a feed zone is identified. Within this zone, a region with the lowest Q_a interval is observed (red ellipse in Fig. 9f). This zone also coincides with a transition to tuffs with veins and vein-dominated crackle breccias. Resistivity increases, pointing at the possibility that quartz alteration is influencing the electrical resistivity log.

5 CONCLUSIONS

Radiative transfer theory separates scattering from intrinsic attenuation of full-waveform sonic logs for two wells in Ngatamariki geothermal field in the Taupo Volcanic Zone, New Zealand. Conventional analysis of the coherent intensities provides only the cumulative effect of scattering and intrinsic attenuation, while Formation Micro Imaging logs have limited resolution and cannot resolve open from mineralized fractures. Results of a 1-D radiative transfer model applied to two geothermal wells identify zones of strong intrinsic attenuation that correlate with high fracture density intervals, known fluid feed zones, and a washout.

For Well 1, the RT separation helps us refine knowledge on three of the six known feed zone intervals, while regions of strong intrinsic attenuation hints at fluid flow just below two other defined feed zones. RT adds more detailed information beyond the conventional well log analysis for all three permeable intervals in Well 2 with well-defined local minima of intrinsic attenuation.

ACKNOWLEDGEMENTS

We thank Mercury NZ Ltd for the financial support for this project and for providing the data and reports from the Ngatamariki geothermal field. We thank Dr. Paul Siratovich for providing feedback on the results, and Dr. Julie Rowland for insightful comments about the geological applications of the attenuation estimates. We also want to thank the editors Dr. Rene-Edouard Plessix and Dr. Herve Chauris for their constructive review of this work.

REFERENCES

Adam, L., Batzle, M., Lewallen, K. & Van Wijk, K., 2009. Seismic wave attenuation in carbonates, *J. geophys. Res.*, **114**(6), doi:10.1029/2008JB005890.

Aki, K. & Chouet, B., 1975. Origin of coda waves: Source, attenuation, and scattering effects, *J. geophys. Res.*, **80**(23), 3322–3342.

Attewell, P.B. & Ramana, Y.V., 1966. Wave attenuation and internal friction as functions of frequency in rocks, *Geophysics*, **31**(6), 1049–1056.

Bakku, S.K., Fehler, M. & Burns, D., 2013. Fracture compliance estimation using borehole tube waves, *Geophysics*, **78**(4), D249–D260.

Biot, M.A., 1956. Theory of propagation of elastic waves in a fluid-saturated porous solid. I. Low-frequency range, *J. acoust. Soc. Am.*, **28**(2), 168–178.

Boseley, C., Bignall, G., Rae, A., Chambefort, I. & Lewis, B., 2012. Stratigraphy and hydrothermal alteration encountered by monitor wells completed at Ngatamariki and Orakei Korako in 2011, in *New Zealand Geothermal Workshop*, Auckland, New Zealand.

Cant, J., 2015. Matrix permeability of reservoir rocks, Ngatamariki Geothermal Field, Taupo Volcanic Zone, New Zealand, *Master's thesis*, University of Canterbury.

Chambefort, I., Lewis, B., Wilson, C., Rae, A., Coutts, C., Bignall, G. & Ireland, T., 2014. Stratigraphy and structure of the Ngatamariki geothermal system from new zircon U-Pb geochronology: implications for Taupo Volcanic Zone evolution, *J. Volcanol. Geotherm. Res.*, **274**, 51–70.

Chandrasekhar, S., 1960. *Radiative Transfer*, Dover Publications.

Chandrasekhar, S., 2013. *Radiative Transfer*, Courier Corporation.

Chapman, M., Liu, E. & Li, X.-Y., 2006. The influence of fluid sensitive dispersion and attenuation on AVO analysis, *Geophys. J. Int.*, **167**(1), 89–105.

Cheng, C. & Toksöz, M., 1981. Elastic wave propagation in a fluid-filled borehole and synthetic acoustic logs, *Geophysics*, **46**(7), 1042–1053.

Cheng, C., Toksöz, M. & Willis, M., 1982. Determination of in situ attenuation from full waveform acoustic logs, *J. geophys. Res.*, **87**(B7), 5477–5484.

Dasios, A., Astin, T.R. & McCann, C., 2001. Compressional-wave Q estimation from full-waveform sonic data, *Geophys. Prospect.*, **49**(3), 353–373.

Dvorkin, J., Mavko, G. & Nur, A., 1995. Squirt flow in fully saturated rocks, *Geophysics*, **60**(1), 97–107.

Fehler, M., Hoshihara, M., Sato, H. & Obara, K., 1992. Separation of scattering and intrinsic attenuation for the Kanto-Tokai region, Japan, using measurements of S -wave energy versus hypocentral distance, *Geophys. J. Int.*, **108**(3), 787–800.

Frehner, M. & Schmalholz, S.M., 2010. Finite-element simulations of stoneley guided-wave reflection and scattering at the tips of fluid-filled fractures, *Geophysics*, **75**(2), T23–T36.

Futterman, W.I., 1962. Dispersive body waves, *J. geophys. Res.*, **67**(13), 5279–5291.

Gamar-Sadat, F., 2015. Automatic gas pocket detection by high-resolution volumetric Q tomography, in *77th EAGE Conference & Exhibition*, Madrid, Spain.

Gamar-Sadat, F., 2016. Image quality enhancement using volumetric q -tomography and q -psdm, in *78th EAGE Conference & Exhibition*, Vienna, Austria.

Gurevich, B. & Pevzner, R., 2015. How frequency dependency of Q affects spectral ratio estimates, *Geophysics*, **80**(2), 39–44.

Halwa, L., 2012. Image Interpretation Report (FMI & AFIT). Mighty River Power Ngatamariki-10, *Tech. rep.*, Schlumberger.

Halwa, L., Wallis, I. & Torres Lozada, G., 2013. Geological analysis of the volcanic subsurface using borehole resistivity images in the Ngatamariki geothermal field, New Zealand, in *35th New Zealand Geothermal Workshop*, Rotorua, New Zealand.

Haney, M.M., van Wijk, K. & Snieder, R., 2005. Radiative transfer in layered media and its connection to the O'Doherty-Anstey formula, *Geophysics*, **70**(1), T1–T11.

Hardin, E., Cheng, C., Paillet, F. & Mendelson, J., 1987. Fracture characterization by means of attenuation and generation of tube waves in fractured crystalline rock at mirror lake, New Hampshire, *J. geophys. Res.*, **92**(B8), 7989–8006.

Herraz, M. & Espinosa, A.F., 1987. Coda waves: a review, *Pure appl. Geophys.*, **125**(4), 499–577.

Hornby, B., Johnson, D., Winkler, K. & Plumb, R., 1989. Fracture evaluation using reflected Stoneley-wave arrivals, *Geophysics*, **54**(10), 1274–1288.

Hornby, B.E., 1989. Imaging of near-borehole structure using full-waveform sonic data, *Geophysics*, **54**(6), 747–757.

Ishimaru, A., 2013. *Wave Propagation and Scattering in Random Media*, Elsevier Science.

Jackson, D.D. & Anderson, D.L., 1970. Physical mechanisms of seismic-wave attenuation, *Rev. Geophys.*, **8**(1), 1–63.

Johnston, D., Toksöz, M. & Timur, A., 1979. Attenuation of seismic waves in dry and saturated rocks: II. Mechanisms, *Geophysics*, **44**(4), 691–711.

Johnston, D.H., 1981. Attenuation: a state-of-the-art summary, in *Seismic Wave Attenuation*, Geophysics reprint series No. 2, eds Toksöz, M. & Johnston, D., SEG.

Jones, I.F., 2013. Absorption related velocity dispersion below a possible gas hydrate geobody, *Geophys. Prospect.*, **61**, 434–445.

- Karpfinger, F., Gurevich, B., Valero, H.-P., Bakulin, A. & Sinha, B., 2010. Tube wave signatures in cylindrically layered poroelastic media computed with spectral method, *Geophys. J. Int.*, **183**(2), 1005–1013.
- Klimentos, T. & McCann, C., 1990. Relationships among compressional wave attenuation, porosity, clay content, and permeability in sandstones, *Geophysics*, **55**(8), 998–1014.
- Knopoff, L., 1964. Q, *Reviews of Geophysics*, **2**(4), 625–660.
- Knopoff, L., Aki, K., Archambeau, C.B., Ben-Menahem, A. & Hudson, J.A., 1964. Attenuation of dispersed waves, *J. geophys. Res.*, **69**(8), 1655–1657.
- Kostek, S., Johnson, D.L. & Randall, C.J., 1998a. The interaction of tube waves with borehole fractures, Part I: Numerical models, *Geophysics*, **63**(3), 800–808.
- Kostek, S., Johnson, D.L., Winkler, K.W. & Hornby, B.E., 1998b. The interaction of tube waves with borehole fractures; Part II, Analytical models, *Geophysics*, **63**(3), 809–815.
- Margerin, L., 2005. *Introduction to Radiative Transfer of Seismic Waves*, pp. 229–252, American Geophysical Union.
- Margerin, L. & Nolet, G., 2003. Multiple scattering of high-frequency seismic waves in the deep earth: PKP precursor analysis and inversion for mantle granularity, *J. geophys. Res.*, **108**(B11), 2514, doi:10.1029/2003JB002455.
- Massiot, C., McNamara, D.D. & Lewis, B., 2013. Interpretative review of the acoustic borehole image logs acquired to date in the Wairakei-Tauhara Geothermal Field, *Tech. rep.*, GNS Science.
- Massiot, C., McNamara, D.D. & Lewis, B., 2015. Processing and analysis of high temperature geothermal acoustic borehole image logs in the Taupo Volcanic Zone, New Zealand, *Geothermics*, **53**, 190–201.
- Massiot, C., McLean, K., McNamara, D., Sepulveda, F. & Milicich, S., 2017. Discussion between a reservoir engineer and a geologist: permeability identification from completion test data and borehole image logs integration, in *39th New Zealand Geothermal Workshop*, Rotorua, New Zealand.
- Mavko, G. & Jizba, D., 1991. Estimating grain scale fluid effects on velocity dispersion in rocks, *Geophysics*, **56**(12), 1940–1949.
- Mayor, J., Margerin, L. & Calvet, M., 2014. Sensitivity of coda waves to spatial variations of absorption and scattering: Radiative transfer theory and 2-D examples, *Geophys. J. Int.*, **197**(2), 1117–1137.
- McLean, K. & McNamara, D., 2011. Fractures interpreted from acoustic formation imaging technology: Correlation to permeability, in *36th Workshop on Geothermal Reservoir Engineering*, p. 10, Stanford University.
- McNamara, D., Massiot, C., Lewis, B. & Wallis, I., 2015. Heterogeneity of structure and stress in the Rotokawa Geothermal Field, New Zealand, *J. geophys. Res.*, **120**(2), 1243–1262.
- Müller, T., Gurevich, B. & Lebedev, M., 2010. Seismic wave attenuation and dispersion resulting from wave-induced flow in porous rocks - a review, *Geophysics*, **75**(5), 75A147–75A164.
- O'Connell, R.J. & Budiansky, B., 1978. Measures of dissipation in viscoelastic media, *Geophys. Res. Lett.*, **5**(1), 5–8.
- O'Doherty, R.F. & Anstey, N.A., 1971. Reflections on amplitudes, *Geophys. Prospect.*, **19**(3), 430–458.
- Oldenburg, D., Scheuer, T. & Levy, S., 1983. Recovery of the acoustic impedance from reflection seismograms, *Geophysics*, **48**(10), 1318–1337.
- Paaschens, J. C.J., 1997. Solution of the time-dependent Boltzmann equation, *Phys. Rev. E*, **56**, 1135–1141.
- Parra, J.O., Xu, P.C. & Hackert, C.L., 2007. A borehole-model-derived algorithm for estimating QP logs from full-waveform sonic logs, *Geophysics*, **72**(4), E107–E117.
- Pevzner, R., 2016. Scattering attenuation from the coal seams in the Cooper Basin, Australia, in *78th EAGE Conference & Exhibition*, Vienna, Austria.
- Pride, S., Berryman, J. & Harris, J., 2004. Seismic attenuation due to wave-induced flow, *J. geophys. Res.*, **109**(1), B01201 1–19, doi:10.1029/2003JB002639.
- Pride, S.R. et al., 2003. Permeability dependence of seismic amplitudes, *Leading Edge*, **22**(6), 518–525.
- Rickett, J., 2006. Integrated estimation of interval-attenuation profiles, *Geophysics*, **71**(4), A19–A23.
- Rickett, J., 2007. Estimating attenuation and the relative information content of amplitude and phase spectra, *Geophysics*, **72**(1), R19–R27.
- Riedel, M., Bellefleur, G., Mair, S., Brent, T.A. & Dallimore, S.R., 2009. Acoustic impedance inversion and seismic reflection continuity analysis for delineating gas hydrate resources near the Mallik research sites, Mackenzie Delta, Northwest Territories, Canada, *Geophysics*, **74**(5), B125–B137.
- Rutherford, S.R. & Williams, R.H., 1989. Amplitude-versus-offset variations in gas sands, *Geophysics*, **54**(6), 680–688.
- Sato, H. & Fukushima, R., 2013. Radiative transfer theory for the fractal structure and power-law decay characteristics of short-period seismograms, *Geophys. J. Int.*, **195**(3), 1831–1842.
- Sato, H. & Hayakawa, T., 2014. Radiative transfer theory for a random distribution of low velocity spheres as resonant isotropic scatterers, *Geophys. J. Int.*, **199**(1), 41–59.
- Sato, H. & Nishino, M., 2002. Multiple isotropic-scattering model on the spherical earth for the synthesis of Rayleigh-wave envelopes, *J. geophys. Res.*, **107**(B12), 2343.
- Schuster, A., 1905. Radiation through a foggy atmosphere, *J. Astrophys.*, **21**, 1–22.
- Shapiro, S.A., Zien, H. & Hubral, P., 1994. A generalized odohertyanste formula for waves in finely layered media, *Geophysics*, **59**(11), 1750–1762.
- Sinev, A. & Podbereznyy, M., 2013. Absorption characteristics of a stoneley wave in multilayered media and the logging method for estimating permeability, *Russ. Geol. Geophys.*, **54**(7), 734–742.
- Spencer, J.W. & Nur, A.M., 1976. The effect of pressure, temperature and pore water on velocities in Westerly granite, *J. geophys. Res.*, **81**, 899–904.
- Stoney, R., 1924. Elastic waves at the surface of separation of two solids, *Proc. R. Soc. A*, **106**(738), 416–428.
- Tang, X. & Cheng, C., 2004. Quantitative Borehole Acoustic Methods, *Handbook of Geophysical Exploration Series*, Elsevier.
- Tang, X.M. & Cheng, C.H., 1989. A dynamic model for fluid flow in open borehole fractures, *J. geophys. Res.*, **94**(B6), 7567–7576.
- Toksöz, M., Johnston, D. & Timur, A., 1979. Attenuation of seismic waves in dry and saturated rocks: I. Laboratory measurements, *Geophysics*, **44**(4), 681–690.
- Toverud, T. & Ursin, B., 2005. Comparison of seismic attenuation models using zero-offset vertical seismic profiling (VSP) data, *Geophysics*, **70**(2), F17–F25.
- Van Der Baan, M., 2001. Acoustic wave propagation in one dimensional random media: the wave localization approach, *Geophys. J. Int.*, **145**(3), 631–646.
- van Wijk, K., 2003. Multiple scattering of surface waves, *PhD thesis*, Colorado School of Mines.
- Vinci, C., Renner, J. & Steeb, H., 2014. On attenuation of seismic waves associated with flow in fractures, *Geophys. Res. Lett.*, **41**(21), 7515–7523.
- Wallis, I., McCormick, S., Sewell, S. & Boseley, C., 2009. Formation assessment in geothermal using wireline tools – application and early results from the Ngatamariki geothermal field, New Zealand, in *31st New Zealand Geothermal Workshop*, Rotorua, New Zealand.
- Wallis, I., McNamara, D., Rowland, J. & Massiot, C., 2012. The nature of fracture permeability in the Greywacke basement at Kawerau Geothermal Field, New Zealand, in *37th Workshop on Geothermal Reservoir Engineering*, Stanford University, Stanford, CA.
- Walsh, J.B., 1966. Seismic wave attenuation in rock due to friction, *J. geophys. Res.*, **71**(10), 2591–2599.
- Wilson, C., Gravley, D., Leonard, G. & Rowland, J., 2009. Volcanism in the central Taupo Volcanic Zone, New Zealand: tempo, styles and controls, *Spec. Publ. IAVCEI*, **2**, 225–247.
- Wilson, C. J.N., Houghton, B.F., McWilliams, M.O., Lanphere, M.A., Weaver, S.D. & Briggs, R.M., 1995. Volcanic and structural evolution of Taupo Volcanic Zone, New Zealand: a review, *J. Volcanol. Geotherm. Res.*, **68**(1–3), 1–28.
- Winkler, K., Nur, A. & Gladwin, M., 1979. Friction and seismic attenuation in rocks, *Nature*, **277**, 528–531.
- Winkler, K.W., Liu, H.-L. & Johnson, D.L., 1989. Permeability and borehole stoneley waves: Comparison between experiment and theory, *Geophysics*, **54**(1), 66–75.

Wu, R., 1993. Separation of scattering and absorption in 1-D random media from spatio-temporal distribution of seismic energy, in *SEG Technical Program Expanded Abstracts 1993*, chap. 275, pp. 1014–1017, The Society of Exploration Geophysicists.

Wyllie, M. R.J., Gardner, G. H.F. & Gregory, A.R., 1962. Studies of elastic wave attenuation in porous media, *Geophysics*, **27**(5), 569–589.

APPENDIX A: COHERENT INTENSITY OF A CAUSAL SOURCE

The coherent intensity (CI) for an impulse response given by the Green's function is:

$$CI \propto \exp(-vt\alpha)\delta(x - vt), \quad \text{where } \alpha = R/l_s + 1/l_a,$$

$$CI \propto \exp(-vt\alpha)\delta\left(t - \frac{x}{v}\right), \quad \text{since } \delta(ax) = \frac{1}{|a|}\delta(x), \quad (\text{A1})$$

let $s(t)$ be a causal source function, then the convolution is given by

$$CI(x, t) * s(t) = \int \delta\left(\left(t - \frac{v}{x}\right) - \tau\right) \exp(-\alpha v(t - \tau))s(\tau)d\tau,$$

$$CI(x, t) * s(t) = \int \delta\left(\left(t - \frac{v}{x}\right) - \tau\right) \exp(-\alpha v\tau) \exp(\alpha v\tau)s(\tau)d\tau \quad (\text{A2})$$

let $\exp(\alpha v\tau) = \omega(\tau)$, then:

$$CI(x, t) * s(t) = \exp(-\alpha vt) \int \delta\left(\left(t - \frac{v}{x}\right) - \tau\right) \omega(\tau)d\tau,$$

$$= \exp(-\alpha vt) \omega\left(t - \frac{x}{v}\right),$$

$$= \exp(-\alpha vt) \exp\left(\alpha v\left(t - \frac{x}{v}\right)\right) s\left(t - \frac{x}{v}\right),$$

$$= \exp(-\alpha x) s\left(t - \frac{x}{v}\right),$$

$$CI(x, t) * s(t) = \exp\left(-x\left(\frac{R}{l_s} + \frac{1}{l_a}\right)\right) s\left(t - \frac{x}{v}\right), \quad (\text{A3})$$

which is a shifted version of the causal response (wavelet) times an exponential decay dependent on the offset and the mean-free paths for scattering and intrinsic attenuation.

APPENDIX B: ERROR PROPAGATION

The receiver closest to the source contains the most information about the incoherent coda (the coherent intensity arrives—and passes the receiver—the earliest). Even for this receiver, Fig. 4 indicates that the intensity at the end of the recording at $t = 5.12$ ms is still well above the background noise level, as defined by the measured intensity prior to the P -wave arrival. If longer times were measured a longer decaying coda would have been recorded. For slow-decaying incoherent energy, longer recordings would provide more stable estimates of l_s , and indirectly in l_a . We therefore recommend longer recordings in future experiments to increase precision in parameter estimation.

The errors represented in Figs 5 and 6 depend on the parameters and errors associated to l_s , l_a , v and α . Errors in v and α are the product of fitting the decay of the maxima of coherent intensity with time and offset respectively as shown in Fig. 3. The square root of the least-squares variance fluctuates depending on the quality of the recorded waveforms and the averaging of the ensemble over a common geology or set of heterogeneities. The errors on the quality factors are obtained from the error propagations on eqs (5). Q_a , which is dependent on l_a , has large associated errors

(above 30 per cent) as a result of the involved equations. The uncertainty on l_s comes from the nonlinear fitting algorithm and was calculated as the standard deviation of the parameter from the matrix of covariances.

The following formulas show the expressions for the errors of l_a and the quality factors:

$$l_a = \frac{1}{\alpha - R/l_s},$$

$$\Delta l_a = l_a^2 \sqrt{(\Delta\alpha)^2 + \left(\frac{R}{l_s} \Delta l_s\right)^2}, \quad (\text{B1})$$

where $\Delta\alpha$ and Δl_s come from the standard deviation of the least-squares fitting. From eq. (B1), a large variance in the total decay α translates to a large variance on the intrinsic absorption mean-free path l_a :

$$\Delta Q_s = Q_s \sqrt{\left(\frac{\Delta l_s}{l_s}\right)^2 + \left(\frac{\Delta v}{v}\right)^2}, \quad (\text{B2})$$

$$\Delta Q_a = Q_a \sqrt{\left(\frac{\Delta l_a}{l_a}\right)^2 + \left(\frac{\Delta v}{v}\right)^2}, \quad (\text{B3})$$

$$\Delta Q_t = Q_t^2 \sqrt{\left(\frac{\Delta Q_s}{Q_s}\right)^2 + \left(\frac{\Delta Q_a}{Q_a}\right)^2}. \quad (\text{B4})$$

APPENDIX C: ENSEMBLE SIZE

The RT analysis requires ensemble averaging to estimate the coherent and incoherent intensities. The assumption is that across the ensemble, the scattering and absorption properties are stationary. Tests on the size of the ensemble from 1.22 m (8 waveforms) to 6.1 m (40 waveforms) prove robustness in our estimates of Q .

Ensembles, theoretically, can be of any length. The main assumption is that the direct (coherent) and scattering energy are equally represented at every receiver in the ensemble. Practically, this means that ensembles should be chosen over a common geology, more precisely, common heterogeneities. When choosing an ensemble size in a volcanic setting we are selecting a section of rock comprising a combination of clasts, fractures and layering with different levels of alteration. Choosing the length of an ensemble should be guided first by our particular interest in geological intervals and those relevant characteristics that could be captured by the elastic wavefield.

Fig. C1 compares Q estimations for different ensemble sizes. The averaging effect of increasing the ensemble size results in smoothing of Q with depth, losing geological details in the log. The estimation using 16 waveforms (2.44 m) per ensemble (blue line) has larger resolution than the more smoothed estimates using one hundred (15.4 m) (cyan line) waveforms.

So far, our Q estimates are for ensembles of 2.44 m length (i.e. 16 sonic waveforms). The number of waveforms composing an ensemble is a choice guided by our geology knowledge, but Fig. C1, shows the stability of the group velocity and attenuation parameters for ensembles from 2.44 to 15.4 m.

C1 Formation Imaging Tool

The FMI and the Borehole Televiewer (BHTV) are used to investigate the heterogeneity and fracture distributions on and near the borehole wall. Their depth of penetration and ability to estimate the type of fractures (induced versus natural) is more limited than our proposed RT methodology. The FMI tool consists of a pad of 192

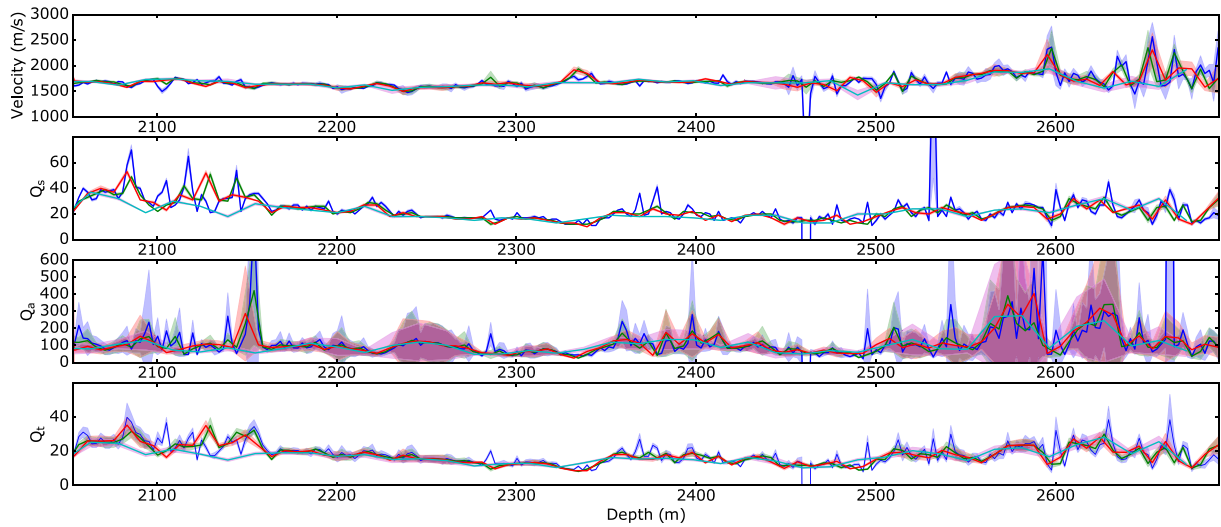


Figure C1. Effect of ensemble size on the estimations for Well 1. Ensembles of 2.44 m (blue), 4.88 m (green), 7.32 m (red) and 15.4 m (cyan). For the geological interpretation we used the smallest ensemble size (2.44 m or 16 consecutive waveforms from the FWSL tool).

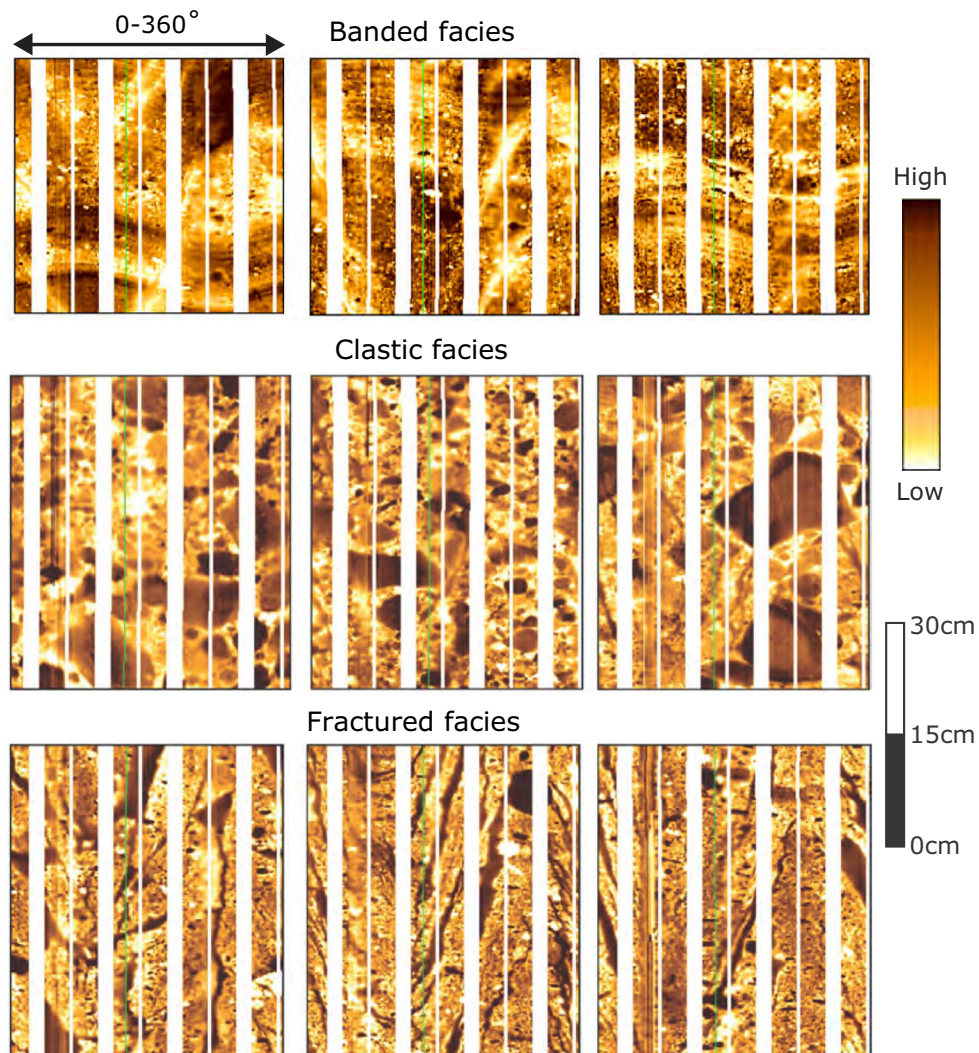


Figure C2. Formation Micro Imager examples of the banded (top), clastic (middle) and fractured (bottom) facies encountered in the pyroclastic section of Well 1 (after Halwa 2012; Halwa *et al.* 2013). The colour scale represents electrical conductivity.

electrodes which detects the electric current flow sent by an upper electrode into the rock formations. This combination of electrodes generates an electrical image of the borehole wall with a resolution of 5 mm (Halwa 2012).

At Ngatamariki, buildup of excess current along a conductive fracture is interpreted as the result of either water or conductive cements—containing pyrite and magnetite—in the fracture causing the current to pool along its trace. Researchers have tried linking acoustic well logging tools to permeability in New Zealand geothermal fields (McLean & McNamara 2011; Wallis *et al.* 2012; Massiot *et al.* 2013; McNamara *et al.* 2015). For example, BHTV data were collected in the Rotokawa Andesite. Rotokawa is an analogous geothermal field south of Ngatamariki and the interpretations on possible open fractures there are not conclusive (McNamara *et al.* 2015). According to McLean & McNamara (2011) and Massiot *et al.* (2017), the integration of image logs interpretation with completion test data (i.e. injection, temperature and spinner profiles) can result in the refinement of feed zone locations. Massiot *et al.* (2017) point out, however, that image logs are unable to confidently identify fluid flowing versus mineralized fractures. Massiot *et al.* (2015) also remind us that an inherent limitation of all BHTV log interpretation is their inability to assess structural connectivity away from the borehole surface and the structure contribution to well per-

meability. This is where our analysis of the full waveform sonic log provides additional information. RT in 1-D on the FWSL may help us separate open from mineralized fractures, as well as fractures below the tool resolution. Intrinsic attenuation is controlled by fluid flow, which is directly related to rock permeability and fluid viscosity (Klimentos & McCann 1990; Pride *et al.* 2004; Müller *et al.* 2010). As the fluid at the depths of interest is water, we hypothesize that the relative variations in intrinsic attenuation (Q_a) are due to changes in rock permeability alone.

An FMI log in Well 1 is used to interpret fracture information in the Tahorakuri Formation and Ngatamariki Andesite (Halwa 2012; Halwa *et al.* 2013). Fig. C2 presents FMI images of typical geological features encountered in the pyroclastic and volcanoclastic section (Tahorakui Formation). Textural features are clasts, bands, laminations and fractures. The clast diameter ranges in size from small (<5 cm) to large (>10 cm), with good sorting for the smaller clasts to moderate for the larger ones. The banding occurs in the andesitic flows while laminations are interpreted in the pyroclastic and volcanoclastic deposits. An FMI image provides information about geometry and electrical current flow into clasts and fractures, but it is not definitive in separating open water-saturated fractures from impermeable ones filled with conductive minerals (e.g. clays).